

A three-dimensional magnetometer for motion sensing of a balloon-carried atmospheric measurement package

R. G. Harrison, G. W. Rogers, and R. J. Hogan

Citation: *Rev. Sci. Instrum.* **78**, 124501 (2007); doi: 10.1063/1.2815349

View online: <http://dx.doi.org/10.1063/1.2815349>

View Table of Contents: <http://rsi.aip.org/resource/1/RSINAK/v78/i12>

Published by the [American Institute of Physics](#).

Related Articles

Transmission of subhertz electromagnetic waves from an inhomogeneous earth's crust to the atmosphere
J. Appl. Phys. **110**, 084910 (2011)

Multijoule scaling of laser-induced condensation in air
Appl. Phys. Lett. **99**, 141103 (2011)

Transmission and total reflection of subhertz electromagnetic waves at the earth-atmosphere interface
J. Appl. Phys. **108**, 124901 (2010)

Nonlinear longitudinal compression of short laser pulses in the atmosphere
Phys. Plasmas **16**, 053104 (2009)

Effects of atmospheric turbulence on remote optimal control experiments
Appl. Phys. Lett. **92**, 041103 (2008)

Additional information on *Rev. Sci. Instrum.*

Journal Homepage: <http://rsi.aip.org>

Journal Information: http://rsi.aip.org/about/about_the_journal

Top downloads: http://rsi.aip.org/features/most_downloaded

Information for Authors: <http://rsi.aip.org/authors>

ADVERTISEMENT



AIPAdvances

Submit Now

**Explore AIP's new
open-access journal**

- **Article-level metrics
now available**
- **Join the conversation!
Rate & comment on articles**

A three-dimensional magnetometer for motion sensing of a balloon-carried atmospheric measurement package

R. G. Harrison,^{a)} G. W. Rogers, and R. J. Hogan

Department of Meteorology, University of Reading, P.O. Box 243, Earley Gate, Reading, Berkshire, RG6 6BB, United Kingdom

(Received 22 August 2007; accepted 29 October 2007; published online 18 December 2007)

An instrument is described which carries three orthogonal geomagnetic field sensors on a standard meteorological balloon package, to sense rapid motion and position changes during ascent through the atmosphere. Because of the finite data bandwidth available over the UHF radio link, a burst sampling strategy is adopted. Bursts of 9 s of measurements at 3.6 Hz are interleaved with periods of slow data telemetry lasting 25 s. Calculation of the variability in each channel is used to determine position changes, a method robust to periods of poor radio signals. During three balloon ascents, variability was found repeatedly at similar altitudes, simultaneously in each of three orthogonal sensors carried. This variability is attributed to atmospheric motions. It is found that the vertical sensor is least prone to stray motions, and that the use of two horizontal sensors provides no additional information over a single horizontal sensor. © 2007 American Institute of Physics. [DOI: 10.1063/1.2815349]

I. INTRODUCTION

Air turbulence occurs on small and large scales in the atmosphere and can present a severe hazard to aircraft. It is often associated with weather systems, but there are also reports of its occurrence away from major zones of disturbance, for example, at high levels.¹ Beneath clouds containing ice, turbulence can result from the cooling associated with the evaporation of ice particles.² There are few *in situ* methods to detect turbulence; however, the terrestrial magnetic field provides a stable reference against which turbulent motions generated in flight can be measured.³ Using the geomagnetic field as a reference, a single geomagnetic sensor added to a standard balloon-carried instrument package for meteorological soundings has been demonstrated to provide high frequency motion detection in turbulent regions of clouds.⁴ High frequency motion within the airflow is sensed directly, alongside the thermodynamic parameters of temperature, pressure, and humidity. As well as turbulent motion detection in the terrestrial atmosphere, the behavior of remote measurement packages in planetary atmospheres, such as the descent of the Huygens probe to Titan,⁵ requires interpretation of probe motions.

To investigate the relative advantages of different sensor combinations and orientation,^{6,7} a three-component orthogonal magnetometer motion sensing system is evaluated here, mounted within a Vaisala RS80 atmospheric radio sounding package (radiosonde). RS80 radiosondes, and their successors, are commonly used in Europe. The radiosonde is carried aloft by a helium filled balloon, and returns to the surface by parachute after the balloon bursts.

II. SYSTEM DESCRIPTION

The three-component magnetometer is integrated with a four-channel data acquisition system⁸ for the Vaisala RS80 radiosonde. The radiosonde data acquisition system provides regulated power supplies, analog-to-digital conversion (5 V unipolar at 12 bit resolution), data formatting, and digital telemetry, which is transmitted to ground over the radiosonde's UHF (403 MHz) radio link. As radiosondes are disposable and only rarely recovered, the three-component magnetometer system is required to be inexpensive and lightweight.

A. Sensor characteristics and temperature stability

The three magnetic sensors employed are Hall effect devices, type SS495 (Honeywell). These have a magnetic sensitivity of (3.125 ± 0.125) mV per 100 μ T, which is suitable for measuring the geomagnetic field (~ 20 μ T horizontally). As the sensor outputs require amplification to suit the resolution (1.2 mV) of the digitization system, it is necessary to establish that thermal drift will not cause the sensor voltages to stray beyond the available measurement range (0 to +5 V).

Temperatures during a radiosonde flight can fall to at least -60 °C, which is colder than the SS495's minimum working temperature of -40 °C specified by the manufacturer. To evaluate possible thermal errors, a large sample of SS495 sensors was investigated over a range of temperatures. The temperature stability of the sensors was evaluated in experiments extending from 10 to -60 °C, using a single operational amplifier gain stage. For each sensor, the temperature drift was found from the gradient of a linear fit between temperature and mean sensor output over the extended temperature range. It was found that the sensors operated reliably over the full temperature range, with a median

^{a)}Electronic mail: r.g.harrison@reading.ac.uk.

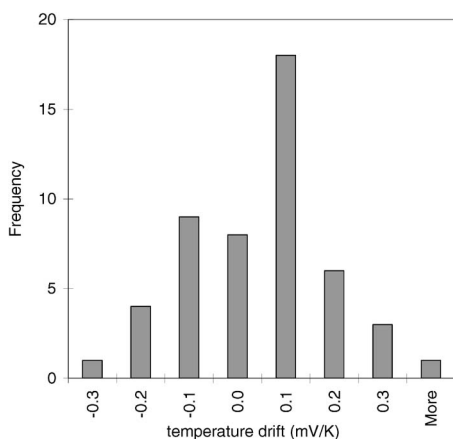


FIG. 1. Histogram of temperature drifts over the range 10 to -60°C , obtained from a sample of 50 SS495A1 Hall effect sensors, measured individually.

temperature drift at the sensor output of 0.1 mV K^{-1} per device. Results of the temperature tests are given in Fig. 1.

B. Sampling rate and telemetry considerations

To detect turbulent motions in atmospheric air, rapid sampling is generally required. For a balloon-carried instrument, a wide range of the turbulent time scales and length scales will be encountered during a flight between the surface and burst point near the tropopause, with the most rapid sampling requirements in the lower atmosphere close to the surface. Length scales of turbulence increase with altitude, but, within a few meters of the surface, sampling rates of 10–100 Hz are required to resolve turbulence, depending on the surface type.⁹ At altitudes of 100–1300 m, turbulence length scales are of order 10–100 m.¹⁰ For wind speeds of order 10 ms^{-1} , the associated time scales are 1 and 10 s, requiring minimum sampling rates of 2 and 0.2 Hz, respectively. A minimum sampling rate of 2 Hz was therefore made the specification to resolve turbulent motions generated during the lower atmosphere ascent.

The data telemetry from the radiosonde's data acquisition system uses the Bell 202 modem standard, at 300 Bd (baud). This is the maximum data rate which does not interfere with the standard meteorological sensor data sent over the same single channel radio link. In the original data acquisition system, the samples were made and sent continuously as serial data over the radio link. The 300 Bd data rate is slow, however, and corresponds to about 30 8-bit characters per second having stop and parity bits. Using three channels, with up to four ascii characters to represent a single measurement, one further character acting as channel separator and a final character to mark the end of line, it is clear that the maximum possible data telemetry rate is about two samples per second on three channels. As processing time is also required to make the samples, the actual sampling rate is less than this. Because the telemetry rate determines the time available for sampling, the high frequency ($>1\text{ Hz}$) information from the attached sensors is lost. A binary transmission method was attempted to reduce the number of characters sent. This achieved approximately double the telemetry rate, but the fixed processing time requirement limited further im-

provements beyond this. Unfortunately, the binary method could fail completely when the radio signal was poor, as, unlike the plain ascii characters data transmission, corrupted binary data were not amenable to simple data recovery. This is an important consideration for an instrument operating in bad weather conditions, as the relative alignment of transmitting and receiving antenna will vary and the received signal strength will fluctuate as a result.

To achieve a higher sampling rate with good data telemetry reliability using plain ascii, a different approach was adopted. This used on-board data storage, to allow measurements to be made at a higher sampling rate which was independent of the data telemetry rate. Effectively, this provides a “burst-mode” method, in which samples are taken rapidly in one burst and then transmitted at a slower rate in a subsequent burst. Only the repetition rate of the bursts is determined by the telemetry rate. For the microcontroller used, additional processing time was required in storing and retrieving the data from the memory over a serial data bus, but there was still a useful increase in the sampling rate. A further advantage of this approach was that individual measurements within each group of three samples were much closer to being simultaneous, generally within 0.1 s of each other. As finally implemented, a 4k EEPROM memory was sufficient to store 32 three-channel measurements in a sampling burst lasting 8.9 s (3.6 samples/s) followed by a transmission burst lasting 25 s. A sample number (0.31) was also added as each set of samples was transmitted, to allow missing values to be identified.

C. Circuitry

The magnetic sensor circuit stages were designed to allow for the measured thermal drift. Each sensor is used with a single inverting operational amplifier amplification stage, providing $\times 33$ gain to obtain an overall sensitivity of $1\text{ mV}/\mu\text{T}$ about a mean level of 2.5 V. Rotating a sensor in the horizontal plane produces a typical amplified fluctuation of $\pm 20\text{ mV}$ about 2.5 V, depending on the actual sensor and amplifier calibration. The $\pm 20\text{ mV}$ variation provides the measurement of position fluctuations, which must be resolved by the data acquisition system despite any thermal drift during the radiosonde flight. With an amplifier gain of $\times 33$ and an assumed 80°C temperature change (i.e., the range from 20 to -60°C), the drift will vary between $\pm 0.25\text{ V}$ (minimum, assuming $\pm 0.1\text{ mV K}^{-1}$ per device) and $\pm 0.8\text{ V}$ (maximum, assuming $\pm 0.3\text{ mV K}^{-1}$ per device). The $\pm 20\text{ mV}$ magnetic fluctuations will therefore occur around a mean level of 1.7–3.3 V, depending on the actual electronics temperatures encountered. Although these changes in the mean level are large, the limits still fall well within the 5 V span of the analog-to-digital system. Over this range the system can measure the $\pm 20\text{ mV}$ fluctuations at a resolution of 1.2 mV.

Figure 2 provides a schematic of the circuitry employed, showing the sensors and their interface with the data acquisition system. Each Hall effect sensor (S1, S2, and S3) is followed by a $\times 33$ inverting amplifier stage, using IC1, IC2a, and IC2b; the amplified signal is then fed to the three analog input channels. The sensors are powered from the

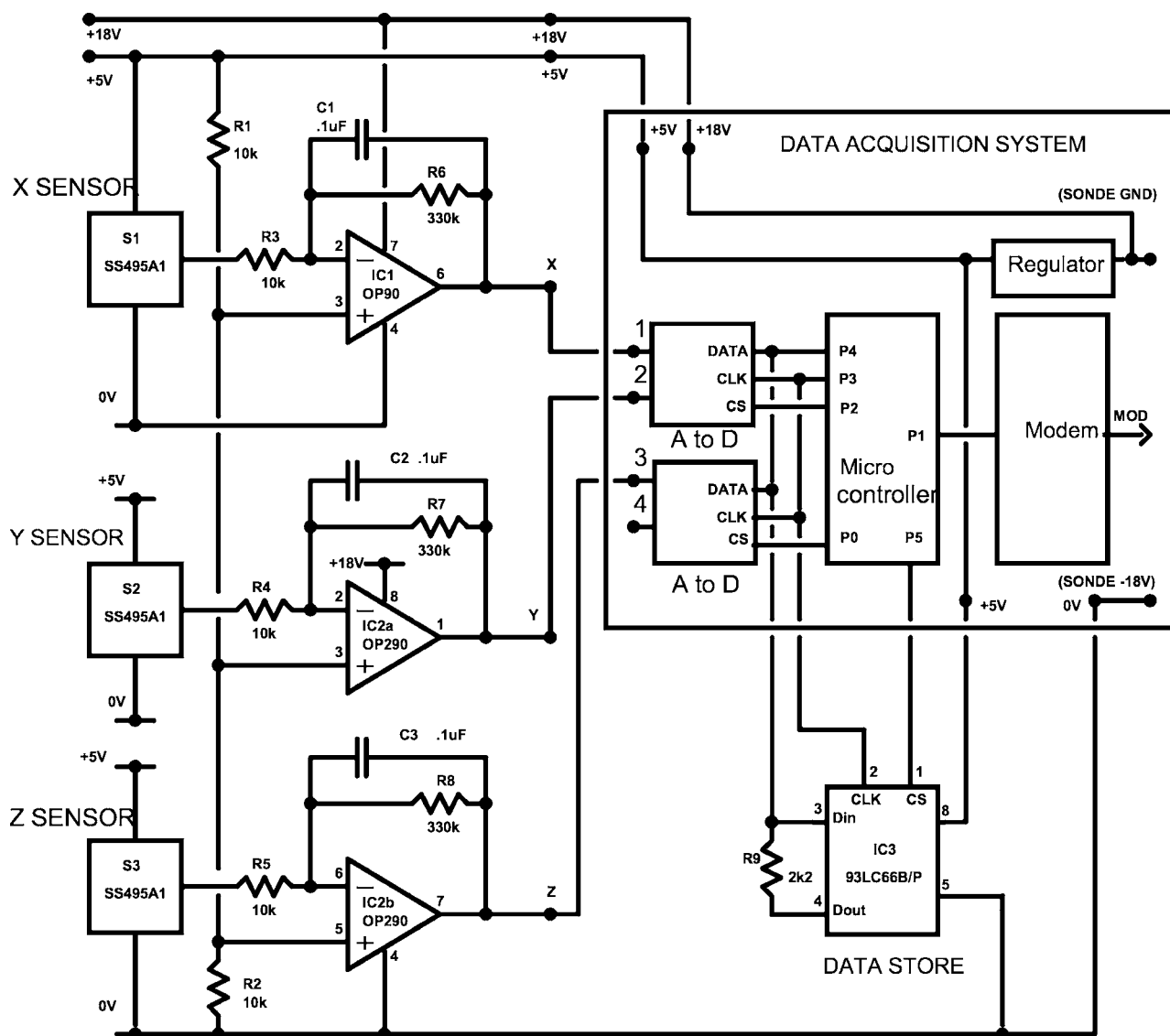


FIG. 2. Schematic of the three-component magnetometer system. The three Hall effect sensors (S1, S2 and S3) and their associated analog signal conditioning (IC1, IC2a, and IC2b) are integrated with a four-channel radiosonde data acquisition system, with an on-board data memory (IC3) added.

regulated +5 V supply furnished by the data acquisition system, but IC1, IC2a, and IC2b are powered from the unregulated +18 V radiosonde battery, to provide a full 5 V signal range from the sensors. A 4k serial memory, IC3, is added to the data acquisition system to provide storage for the burst-mode sampling. It is selected using the microcontroller output P5, and shares the same bidirectional serial data bus and clock lines used for the analog-to-digital stages of the acquisition system.

The three Hall sensors and their amplifiers were mounted within the polystyrene housing of the RS80 radiosonde, on a small circuit board. S1 and S2 were mounted orthogonally in the horizontal plane, and S3 to sense in the vertical. Figure 3 shows the axis system with respect to the radiosonde package. The three-component magnetometer sensor circuit board had a mass of 6 g, and the modified data acquisition board a mass of 17 g, contributing in total an additional 10% to the RS80 radiosonde (with battery) mass of 230 g. Current consumption was 20.5 mA for the magnetometer, and 3 mA for the data acquisition board. The com-

ponent cost for the magnetometer sensor board is about £15 (UK pounds).

D. Data recording

As described, the data acquisition system sent bursts of 32 samples from the three channels over the RS80 narrow band frequency modulation radio link. The radio signal was received using a whip antenna with a mast-head preamplifier, and the audio from the attached UHF receiver decoded using a further Bell 202 modem. One laptop computer was used to record and time stamp the serial data from the receiving modem, with a second laptop computer used to record and time stamp the meteorological data retrieved using a Vaisala PP11 sonde processor. The logging programs were written in TURBO PASCAL, with both laptop real-time clocks synchronized before use. The magnetometer data were produced as one separate file per measurement burst, with the simultaneous temperature, pressure, and humidity information added from the meteorological data.

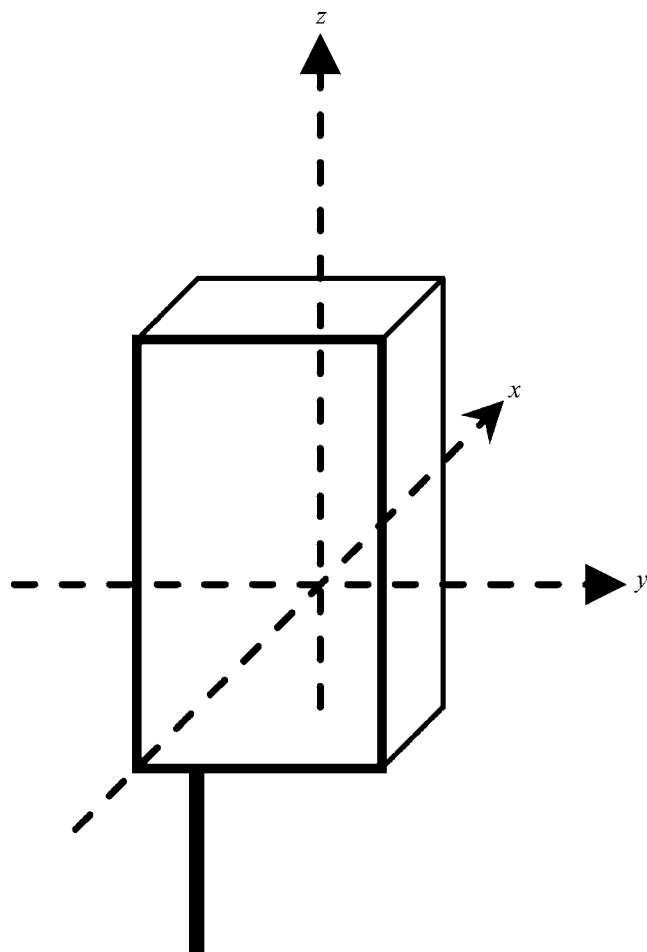


FIG. 3. Geometry of the magnetometer instrument X, Y, Z sensors enclosed within an RS80 meteorological radiosonde (95 mm wide \times 145 mm high \times 60 mm deep). The UHF whip antenna is shown as a thick vertical line beneath the cuboidal radiosonde.

E. Laboratory tests

Simple tests were made on the adequacy of the measurement system by allowing the radiosonde to spin and swing as a pendulum on a 1 m length of string. Figure 4 shows time series from the three-component (x, y, z) magnetometer in each case. With the radiosonde spinning [Fig. 4(a)], the sampling rate is sufficient to show rapid variations in the horizontal (x and y) sensors; in the swinging case [Fig. 4(b)], the motion is slower, but more complicated because of a slow spin also present.

III. ATMOSPHERIC MEASUREMENTS

A series of three atmospheric test ascents was made on 28 October 2006 from Durlston Head (50° 35.7'N, 1° 57.4'W), on the south coast of the UK. For these ascents the radiosonde was attached to a 100 g helium filled balloon, using a 1.7 m length of string. From the surface, several levels of cloud were evident, which changed during the day. High level ice cloud (cirrus) was apparent through gaps in the lower cloud layers.

A. Data processing

From the laboratory tests in which the radiosonde was moved in all possible directions to provide the maximum change, it was clear that the magnetic field could not vary by more than about $\pm 35 \mu\text{T}$ from the median value. This information was used to reject out of range values. It was implemented simply by calculating the median value per measurement burst (from uncalibrated analogue to digital counts, nominally $1.2 \mu\text{T}/\text{count}$), and rejecting all values which fell beyond ± 30 counts from the median, as the median is relatively robust to outliers compared with the mean. With no telemetry failures, the measurement cycle for each sensor should provide 32 samples. Figure 5 shows the distribution of samples received. 65% of the cycles provided all 32 possible samples, 74% provided 30 samples or more, and 96% provided 16 samples or more.

To make the best use of the available values per measurement cycle, the mean analog-to-digital converter count ("ADC counts") and its standard deviation was calculated in each magnetic field direction (x, y, z). The standard deviation provides an estimate of the variability obtained over each measurement cycle, and can be calculated even if some values are missing.

B. Variations with height

Figure 6 shows profiles of the mean ADC counts for the X, Y , and Z sensors for each measurement cycle, and the values shown are plotted against the radiosonde measurement of pressure (a height coordinate) in Fig. 6, for the three ascents. Profiles are also given for temperature and dewpoint temperature, obtained as described previously.¹¹ The closeness of the dewpoint to the air temperature shows that the air was generally moist, except for some dry layers. It is evident from Fig. 6 that the mean ADC count varied strongly with temperature, which depends on the temperature coefficient of the particular sensor in use. As is clear from the results in Fig. 1, the sensor temperature coefficient can have either sign. Figure 6 also includes a measure of the variability in each point, calculated as one standard deviation from the values in each measurement burst.

Since the variability in each of the components provides information on the motion of the radiosonde, Fig. 7 shows the variability plotted against the pressure coordinate. The approach of using the variability is advantageous as it removes the effect of the temperature drift in the mean values of the measurements. The vertical profile of relative humidity (RH) is also given for each ascent, from which it is apparent that regions with larger variability are generally associated with regions of higher RH.

Data from each of the ascents show that the background level of variability is least in the Z sensor. Although greater than that for the Z sensor, the X and Y sensors both have similar variability. All three ascents [Figs. 7(a)–7(c)] show a single layer of enhanced variability in all three (X, Y, Z) magnetometer measurements. The mean height and thickness of the layer vary, during the day, but it is always above about

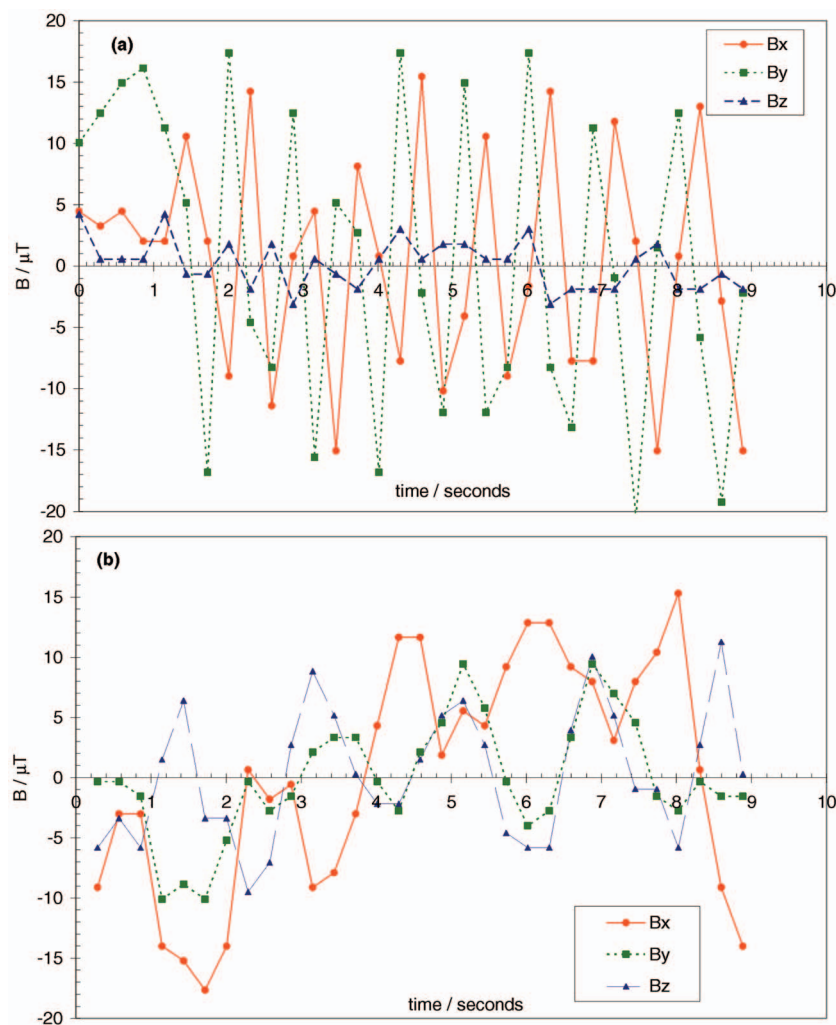


FIG. 4. (Color) Motion of the radiosonde sampled by the three internal sensor (X, Y, Z) measurements of geo-magnetic field (B_x, B_y, B_z) during (a) spinning and (b) swinging.

500 hPa (~ 5 km). The common occurrence of an enhanced variability layer in all three ascents indicates that the atmospheric properties are causing the variability recorded by the sensors, rather than being generated internally within the measurement system. Further evidence supporting the atmospheric generation of motion at this atmospheric level is that both the RH data from the radiosonde and cloud radar observations made simultaneously at Chilbolton (Hampshire, UK, 70 km distant) in similar conditions indicated the presence of an ice cloud layer several kilometers thick.

C. Comparison of orthogonal components

The differences in response between the three sensor directions are compared in Fig. 8. For each ascent simultaneous standard deviations in X , Y , and Z are plotted in pairs, with a local polynomial fit (lowess) added and a one-to-one line. (The lowess line shows if there is a local statistically significant relationship between the variables, or no relationship.) XY plots provide a basic test on the data, as the two sensors are both horizontally aligned, but measuring independently. The XY plots [Figs. 8(a), 8(d), and 8(g)] show

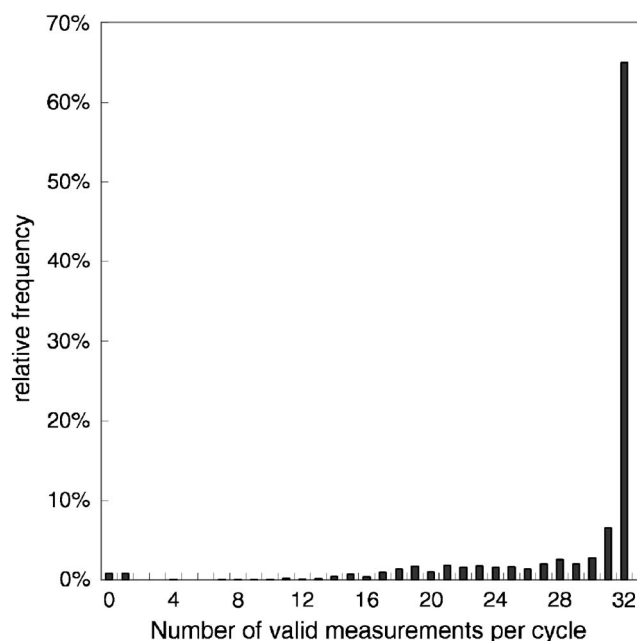


FIG. 5. Histogram of number of valid measurements received per cycle of 32 measurements, rejecting values falling beyond ± 30 counts from the median of the received values, and those for which a finite value could not be retrieved. The histogram was generated from 1743 measurement cycles across the three channels during three flights.

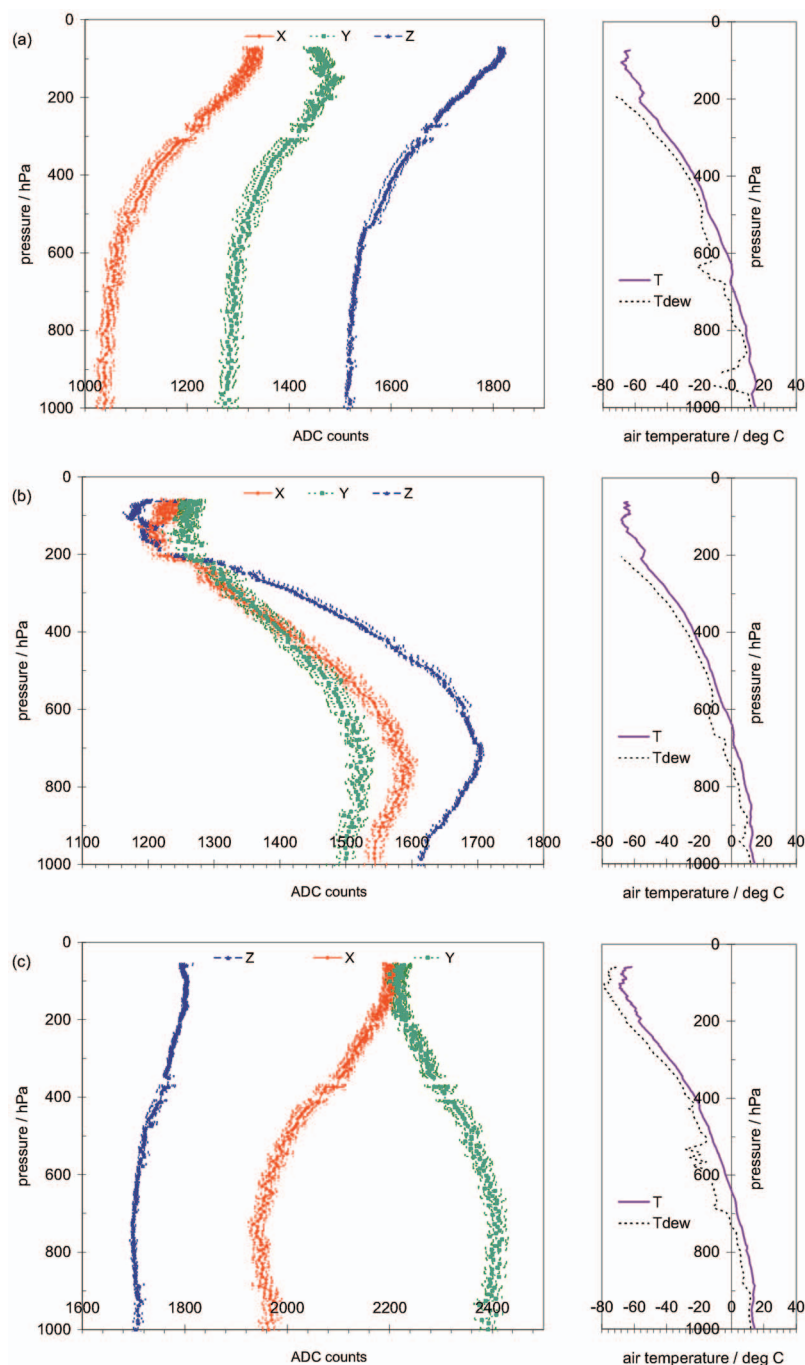


FIG. 6. (Color) Vertical soundings of mean sensor counts (nominally $1.2 \mu\text{T}/\text{count}$), obtained in the x , y , and z directions, with variability of one standard deviation marked from up to 32 samples for each point (left panel), together with the atmospheric temperature (air temperature T and dew point temperature T_{dew}) structure. (Note that 1000 hPa is at the surface, 500 hPa ~ 5 km altitude, and 250 hPa ~ 10 km altitude.) The soundings were made from Durlston Head, Dorset, UK, on 28 October 2006, launched at (a) 0845UT, (b) 1045UT, and (c) 1308UT.

approximately linear relationships between the variability in the two sensors, as the lowest line has a similar gradient to the one-to-one line. The YZ and ZX plots, however, show a nonlinear relationship between the horizontal and vertical sensors. In particular, when the lowest line is close to horizontal on the YZ plots [e.g., Figs. 8(b), 8(e), and 8(h)], there is variability in Y which is associated with minimal variability in Z . The “knee” in the lowest relationship between Y and Z probably marks the transition when the radiosonde begins to spin, which primarily affects the horizontal sensors. This demonstrates that the motion information provided by the vertical sensor differs from that provided by the two horizontal sensors. Because the horizontal (X and Y) sensors are prone to twisting or spinning motions which may be excited by nonturbulent motions such as pendulum oscillations, the

vertical sensor may provide the best signal-to-noise detection of the radiosonde motion⁶ from the three directions available.

D. Signatures in power spectra

Each burst of measurements provides a short time series of data from which a power spectrum can be calculated. This method of analysis identifies the frequencies present in the radiosonde motion. Higher frequencies (> 1 Hz) have previously been associated with turbulent regions of clouds,⁴ using a single horizontally aligned sensor.

A complication in such data analysis is that some values are missing in the time series forming each measurement cycle. The approach adopted to proceed with spectral analysis was to replace the missing values with values selected

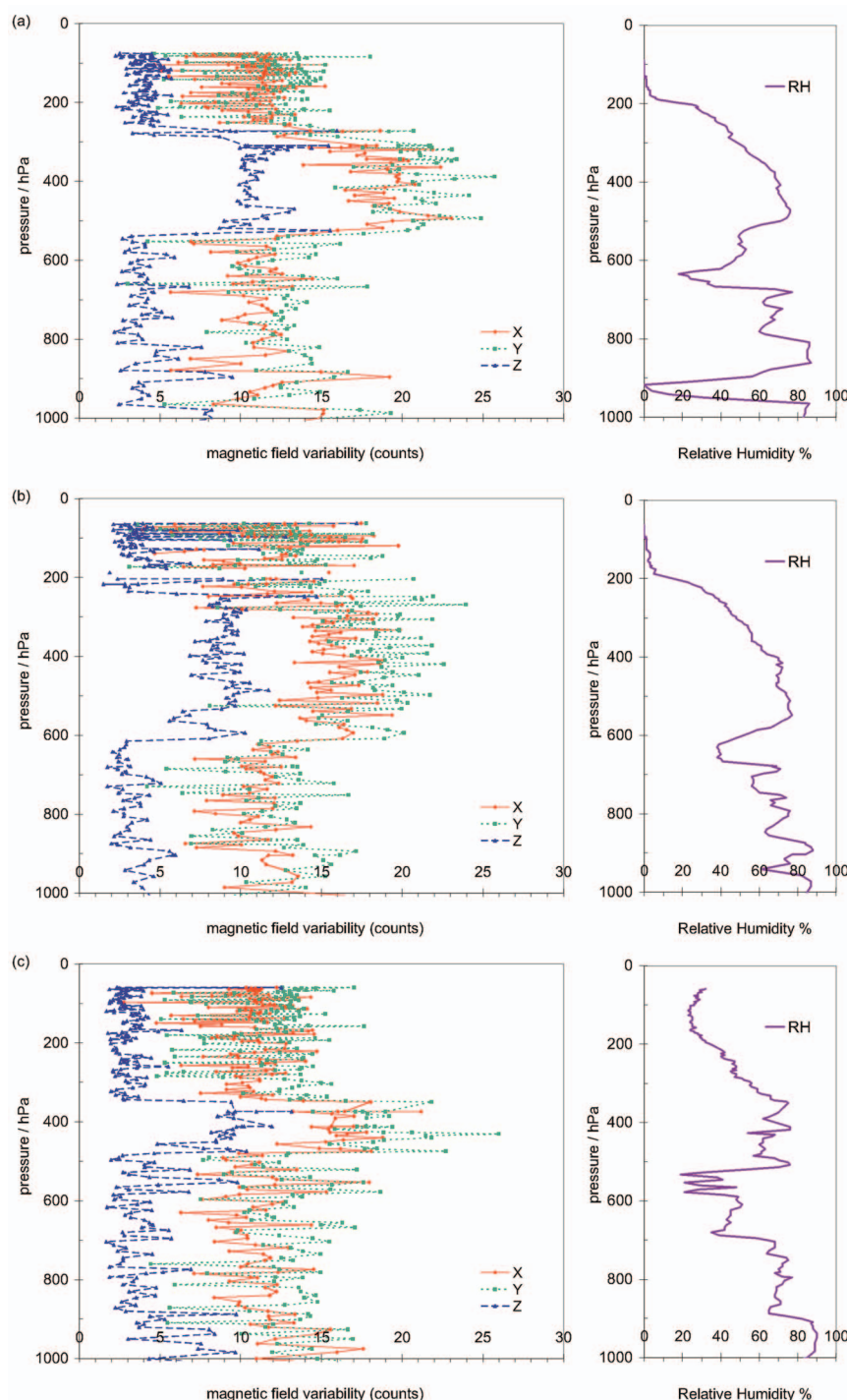


FIG. 7. (Color) Vertical soundings of magnetic variability in the x , y , and z directions from the data in Fig. 6 for 28 October 2006 launches at (a) 0844UT, (b) 1045UT, and (c) 1308UT. The variability shown is one standard deviation (in sensor ADC counts) calculated from nominally 32 samples (left panel). The right panel in each case shows the associated relative humidity (RH) profile.

randomly from the available values. This adds white noise to the data, but should not introduce spectral features. To ensure that the power spectrum obtained was insensitive to the choice of random values, the replacement procedure was repeated many times and the final power spectrum obtained by averaging the individual spectra produced.

Figure 9 provides example time series obtained during all the flights made on 28 October 2006. Figures 9(a) and 9(b) show time series and power spectra for measurements beneath the turbulent layer. All three sensors show small variability (and the Z sensor the least variability), and all the power spectra show no high frequency motion present. Figures 9(c) and 9(d) show measurements from within the tur-

bulent layer and all sensors show more variability than for Figs. 9(a) and 9(b). The power spectra for all three sensors are similar, with higher frequency motions evident at frequencies around 0.5 Hz. Figures 9(e) and 9(f) show a further set of measurements from within the turbulent layer, emphasizing that a range of detailed responses is possible. The horizontal sensors' data show high frequency behavior, which the relevant power spectra showing spectral energy at frequencies >1 Hz. The vertical sensor shows a much slower oscillation, with some spectral energy present at the same frequency as the horizontal sensor. The time series in Figs. 9(e) and 9(f) are also suggestive of the spin (XY) and swing (Z) motions illustrated in Fig. 4.

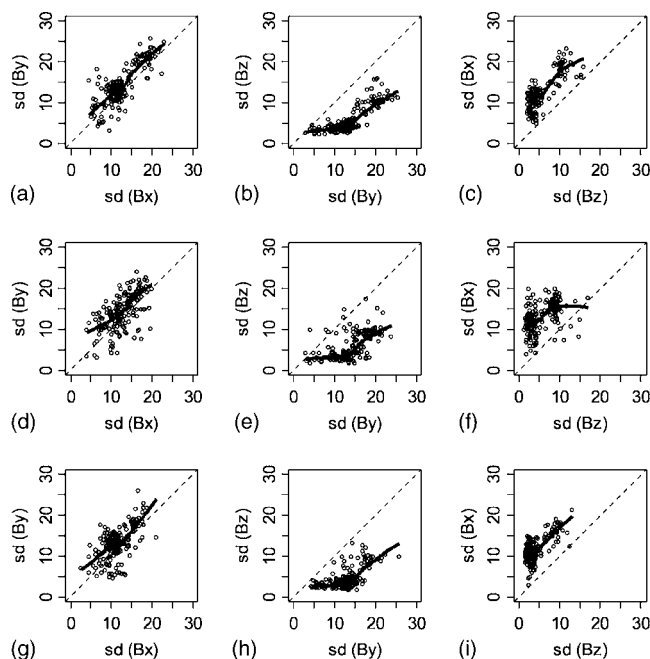


FIG. 8. Standard deviations obtained for each burst of measurements obtained along one axis, plotted against simultaneous standard deviations obtained along an orthogonal axis. A set of three plots (xy , yz , and zx) is given for each of the three flights shown in Fig. 6: [(a)–(c)] 0844UT launch; [(d)–(f)] 1045UT launch, and [(g)–(i)] 1308UT launch. A robust local polynomial (lowess) fit line has been added to each scatter plot, and the one-to-one relationship line is dashed.

E. Deriving rotation rate

Power spectra can be used to derive the rate of rotation in the horizontal plane, which provides an alternative metric of turbulence to the standard deviation of the individual channels shown previously. Two methods are used to estimate average rotation rate from the 32 X and Y samples, after they have each been corrected for temperature drift.

The first method performs fast Fourier Transform (FFT) on the complex time series $V(t) = X(t) + iY(t)$, to derive the power spectrum as a function of rotation rate. A Hanning

window is applied, and, as before, missing values are replaced by random numbers drawn from the distribution of available values, a process that is repeated multiple times to ensure that no spectral features are added. The power spectrum $P(f)$ is defined in the frequency range $-1/2\Delta t < f < +1/2\Delta t$, where Δt ($=0.287$ s) is the sampling interval. (Rotation rates outside this range will be aliased.) To find the mean rotation rate \bar{f} , the peak in the power spectrum is located and the spectrum is reordered so that the peak lies in the center. The mean rotation rate is given by the first moment of the distribution

$$\bar{f} = \int fP(f)df / \int P(f)df \quad (1)$$

The gray line in Fig. 10(a) shows a profile of \bar{f} for the second of the three ascents in Fig. 7. It can be seen that rotation rate is less than 0.6 Hz up to 600 hPa, above which it rapidly increases, fluctuating through the full Nyquist range of ± 1.74 Hz. It is likely that at times the true rotation rate lies outside this range but it is folded back in. The vertical position of the turbulence located by using rotation rate agrees well with the position found from the standard deviation in Fig. 7(b).

The second method for calculating rotation rate is essentially the same as the “pulse-pair” method used by weather radars to derive Doppler velocity from the phases of a sequence of returned pulses from a target.¹² In this method, the mean rotation rate (in Hz) is given by

$$\bar{f} = \frac{1}{2\pi\Delta t} \arg \sum_i V_{i+1}V_i^* \quad (2)$$

where \arg denotes the argument of a complex number in radians, and V^* is the complex conjugate of V . There are three potential advantages of this approach. Firstly, it only requires a running sum of a set of complex multiplications, so in principle it would be possible for the microprocessor carried on the radiosonde to make the calculation. Secondly, it is easy to deal with missing data by removing from the

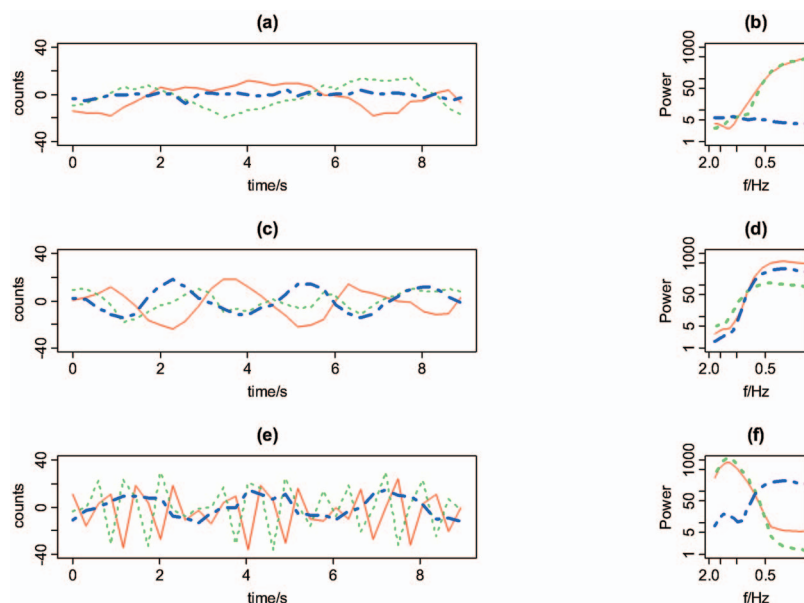


FIG. 9. (Color) Time series from measurement bursts at (a) 847 mbars, (c) 525.3 mbars, and (e) 402.7 mbars, with associated power spectra (b), (d), and (f), respectively. Data from the X sensor are plotted as a solid red line, from the Y sensor a dotted green line, and from the Z sensor a dot-dashed blue line. (The y axis is expressed in analog-to-digital counts, nominally $1.2 \mu\text{T}/\text{count}$, about the median value of the samples.)

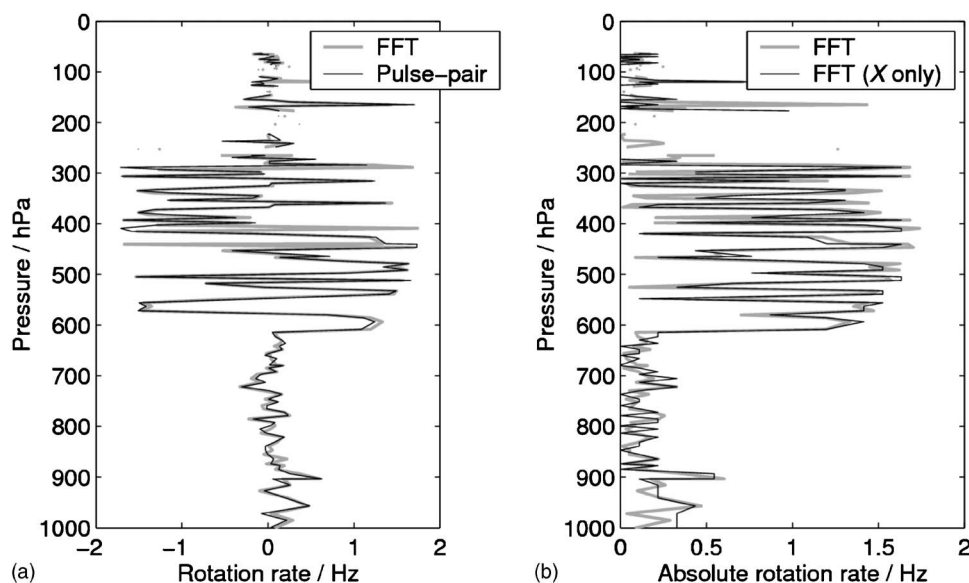


FIG. 10. (a) Rotation rate derived from the X and Y measurements taken during the second of the three ascents, using the FFT and “pulse-pair” methods described in the text. (b) Absolute rotation rate derived using both the X and Y measurements (i.e., the magnitude of the FFT method shown in panel (a) and using only the X measurements).

summation any pairs that include one or two missing values. Thirdly, it does not assume the spectrum to be periodic, as for a Fourier transform. The results of this method are shown by the black line in Fig. 10(a), and exhibit generally good agreement with the FFT method (except between 400 and 450 hPa where the frequencies are close to the “folding” value of ± 1.74 Hz).

Finally, the reliability of mean rotation rate derived with just one of the two horizontally oriented sensors (i.e., X or Y) is investigated. In this case the magnitude but not the sign of rotation rate can be derived. The gray line in Fig. 10(b) shows the absolute rotation rate derived from X and Y, i.e., the magnitude of the gray line in Fig. 10(a). The black line shows absolute rotation rate estimated from X only. Since in this case the power spectrum is not truly periodic, it is not possible to “reorder” the elements as is done for X and Y. Therefore, absolute rotation rate is simply taken as the peak in the X power spectrum. The agreement is sufficiently good to justify only carrying one horizontally aligned sensor.

IV. DISCUSSION

The use of orthogonal sensors with the burst sampling approach provides measurements of radiosonde motion at frequencies up to about 2 Hz, in each of three directions. The data processing techniques developed are resilient to poor telemetry, through calculating the variability in each burst of measurements, and the power spectra.

Using the simultaneous sets of three measurements, it is possible to compare the relative advantages of measurements in the horizontal and vertical directions. Common responses are generated in the horizontal and vertical measurements from atmospheric changes, but use of three sensors is clearly unnecessary. Use of two horizontal sensors (X and Y) does

not provide appreciably more information than a single horizontal sensor operating in either the X or the Y direction. Further, the vertical (Z) sensor is less prone to the effects of twisting, and shows a lower level of background variability than either of the horizontal sensors. A single sensor system should therefore use a vertical sensor, but a dual sensor system should use one horizontal and one vertical sensor. The use of two sensors is desirable as it provides confidence in the results when common features are detected in both sensors, such as a similar vertical variability structure or similar frequency motions.

ACKNOWLEDGMENTS

S. D. Gill assisted with the balloon launches and made the Civil Aviation Authority arrangements. This research was funded by the Paul Instrument Fund of the Royal Society.

- ¹T. Roach, *Meteorol. Mag.* **98**, 1160 (1969).
- ²F. I. Harris, *J. Atmos. Sci.* **34**, 651 (1977).
- ³A. J. Lapworth and P. J. Mason, *J. Atmos. Ocean. Technol.* **5**, 699 (1988).
- ⁴R. G. Harrison and R. J. Hogan, *J. Atmos. Ocean. Technol.* **23**, 517 (2006).
- ⁵R. D. Lorenz, J. C. Zarnecki, M. C. Towner, M. R. Leese, A. J. Ball, B. Hathi, A. Hagermann, and N. A. L. Ghafoor, *Planet. Space Sci.* **55**, 1936–1948 (2007).
- ⁶R. D. Lorenz, *J. Atmos. Ocean. Technol.* **24**, 1520 (2007).
- ⁷R. G. Harrison and R. J. Hogan, *J. Atmos. Ocean. Technol.* **24**, 1521 (2007).
- ⁸R. G. Harrison, *Rev. Sci. Instrum.* **76**, 026103 (2005).
- ⁹J. C. Kaimal and J. J. Finnigan, *Atmospheric Boundary Layer Flows: Their Structure and Measurement* (Oxford University Press, New York, 1994).
- ¹⁰R. J. Taylor, J. Warner, and N. E. Bacon, *Q. J. R. Meteorol. Soc.* **96**, 750 (1970).
- ¹¹R. G. Harrison, *Rev. Sci. Instrum.* **76**, 126111 (2005).
- ¹²R. J. Doviak and D. S. Zrnic, *Doppler Radar and Weather Observations* (Dover Press, New York, 2006), p. 562.